J Mater Sci (2007) 42:495–509
DOI 10.1007/s10853-006-1258-2

Microstructural development and solidification cracking susceptibility of Cu deposits on steel: Part I

Fredrick F. Noecker II · John N. DuPont

Received: 17 June 2004 / Accepted: 13 January 2006 / Published online: 28 December 2006

Abstract The tool and die industry is interested in depositing Cu onto steel using direct metal deposition techniques in order to improve thermal management of mold dies manufactured from steel alloys. However, Cu is a known promoter of solidification cracking in steel. The goal of this work was to identify the range of Cu compositions in steel that cause cracking and understand the cracking susceptibility through analysis and modeling of microstructural development. A wide range of steel–Cu deposits, from approximately 3 to 97 wt% Cu, were fabricated using the gas tungsten arc welding (GTAW) process with cold wire feed. The deposits were found to be crack free when the concentration of Cu was below approximately 5 wt% or above approximately 52 wt%. Cracking was observed in deposits with Cu concentration between approximately 5 and 43 wt%. Thus, to ensure crack free deposition of Cu onto Steel, the concentration of the first layer must be about 52 wt% Cu or greater. The corresponding volume fraction of terminal Cu in samples that cracked was between approximately 0.1 and 27%. The resultant microstructures were characterized by various microscopy techniques to understand the influence of Cu on solidification cracking. Additionally, solidification modeling was undertaken to determine the amount of terminal Cu rich liquid that would form under equilibrium and non-equilibrium solidification conditions.

F. F. Noecker II (✉) · J. N. DuPont
Engineering Metallurgy Group, Department of Materials Science and Engineering, Lehigh University, Bethlehem, PA, USA
e-mail: ffn2us@yahoo.com

Introduction

Tool steel is a widely used mold material due to its favorable mechanical properties, but the thermal conductivity limits the melt cooling rate and increases mold cycle time. The thermal conductivity of copper [1] is approximately 13 times that of AISI H-13 tool steel [2] at operating temperatures between 220 °C and 600 °C. It has been shown that mold cores fabricated from Cu based alloys used in steel molds significantly decrease the cooling times compared to monolithic tool steel [3].

Direct metal deposition (DMD) processes, such as Laser Engineered Net Shaping^{TM} (LENS^{TM}), offer several advantages that make them well suited to fabricate steel molds with Cu cores. LENS^{TM} is a solid free form fabrication process capable of producing fully dense 3-D complex shapes directly from a Computer Aided Design (CAD) drawing. LENS^{TM} utilizes a Nd-YAG laser to produce a melt pool on a substrate attached to an X-Y table. Powder metal from coaxial powder feed nozzles is injected into the melt pool as the table is moved along a pre-designed two dimensional tool path that is ''sliced'' from a three dimensional CAD drawing. A fully dense part is produced by depositing line after line, which are built into sequential layers. LENS has already proven its ability to produce molds out of tool steel [4] and has shown promise in producing conformal cooling channels in molds made out of the same material [5]. Additionally, several researchers have investigated the fabrication of functionally graded materials using DMD variant processes [6–8]. The tool and die industry would like to exploit the LENS process for producing steel–copper functionally

graded conformable cooling channels to improve die thermal management and ultimately increase productivity.

Attempts to deposit copper onto tool steel using the LENS process have been limited in their success primarily due to solidification cracking [9]. Copper has been shown by several researchers to promote solidification cracking/hot cracking in steel [10–13]. Solidification cracking is a function of the solidification temperature range and the amount of terminal liquid, both of which are controlled by the nominal composition and solidification conditions [14–17].

Figure 1 is an Fe–Cu equilibrium phase diagram [18], which displays a large solidification temperature range (ΔT) on the order of several hundred degrees C over a wide range of Cu concentrations along with limited solid solubility of Cu in Fe. Additionally, there are two peritectics, one on the Fe rich side and the other at the Cu rich end of the phase diagram (Fig. 2). The resultant effect on solidification cracking susceptibility is expected to be significant in both equilibrium and non-equilibrium solidification conditions. Under equilibrium solidification conditions (i.e. equilibrium at the solid/liquid interface, no undercooling and infinite diffusion in solid and liquid phases) Fe–Cu alloys with more than approximately 13 wt% Cu will have a solidification temperature range of over approximately 300 °C and produce terminal Cu rich liquid. The unfavorably large solidification temperature range persists up to approximately 85 wt% Cu where the liquidus temperature starts to decrease significantly and causes a considerable reduction in ΔT with increasing Cu. Solidification terminates with a Cu rich phase (~97 wt% Cu) when the liquid composition is enriched to the Cu rich peritectic. Between 8.2 and 14 wt% Cu the retrograde solubility complicates the equilibrium solidification behavior of Fe–Cu alloys. Regardless, the large solidification temperature range over a wide range of Fe–Cu compositions, combined with the formation of a terminal Cu rich liquid is expected to result in a significant solidification cracking susceptibility under equilibrium conditions.

Scheil solidification conditions [19] are similar to equilibrium conditions, except there is no diffusion of solute in the solidifying solid. For Scheil solidification conditions the large solidification temperature range is extended to even lower concentrations of Cu in Fe. Additionally, solidification will terminate at pure Cu even if trace amounts of Cu are added to Fe, therefore the solidification temperature range is ~10 °C greater than equilibrium conditions at any nominal compositions. The limited solid solubility of Cu in Fe will lead to significant amounts of terminal liquid over a similarly large range of nominal compositions. As such, the Fe–Cu system is expected to be inherently crack susceptible over a very large range of nominal compositions for both equilibrium and non-equilibrium solidification conditions. The objective of this work is to identify the concentrations of Cu in steel that result in crack free deposits as an important step towards successfully depositing Cu onto tool steel using DMD techniques.

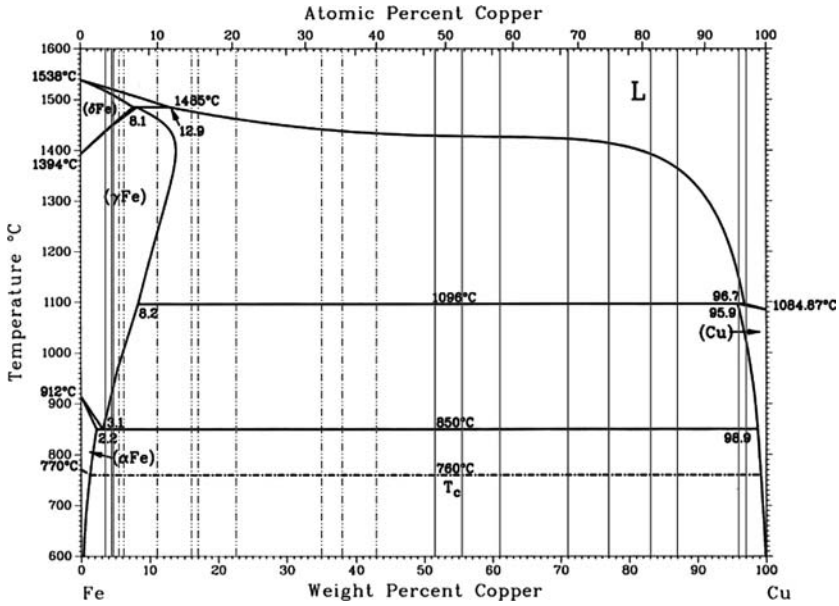

Fig. 1 Fe–Cu equilibrium phase diagram [18] with solidification cracking results. Solid and dashed lines represent crack free and cracked deposits respectively

Experimental procedure

A simplified, yet representative material system consisting of SAE 1013 steel and commercially pure deoxidized (DEOX) Cu were chosen to simplify the analysis while producing results representative of the solidification behavior of tool steel and copper. The compositions of the 1013 Steel and Cu wire are presented in Table 1.

Single pass deposits provide the easiest means to analyze the effects of Cu concentration on solidification cracking. However, single pass deposits produced with the LENS^{TM} process are on the order of only 1 mm in width, making sample preparation and analysis difficult. The current work only considers compositional effects on solidification cracking, therefore a wide range of steel–Cu compositions were fabricated by depositing Cu onto 2.54 cm wide $\times$ 0.635 cm thick AISI 1013 rolled steel bar using a gas tungsten arc weld (GTAW) process with cold wire feed. The GTAW deposits are on the order of 1 cm in width or larger, permitting straight forward sample preparation and analysis, yet still representative of solidification under relatively high cooling rates.

The experimental setup is described in more detail by Banovic et al. [20]. The GTAW processing parameters were as follows: 2.54 mm arc gap, 2 mm/s travel speed, 250 mpere arc current and 10 V arc potential. The shielding gas was commercially pure Ar. The filler metal was 1.143 mm diameter (0.045 in.) deoxidized (DEOX) Cu. The deposit composition was varied by changing the wire feed speed, while all other processing parameters remained constant. Wire feed speed ranged from approximately 2 mm/s to 76 mm/s.

Transverse cross sections of samples from each processing condition were sectioned, mounted, ground and polished using standard metallographic techniques, then etched in 2% Nital. Both bulk and point compositions were determined with an electron-probe microanalyzer (EPMA). A JEOL 733 Super Probe, equipped with wavelength dispersive spectrometers, was operated at an accelerating voltage of 20 kV and a probe current of 25 nA for bulk analysis. To minimize the excitation volume yet maintain sufficient overvoltage to generate CuK_{α} X-rays, the accelerating voltage was reduced to 15 kV for point analysis and line scans. To measure the nominal composition of the deposits three to six measurements were acquired per deposit from an area approximately 2000 μm^2 per measurement. This area was large enough to average out variations in composition due to microsegregation and provide good statistical measurement of the nominal deposit composition. A phi(ρZ) correction method was utilized to convert X-ray counts to weight percentages [21]. Compositional data was normalized for weight percent Fe and Cu, which is reasonable given the maximum amount of trace elements present is 1.36 wt%. For deposits with nominal Cu concentrations greater than 71 wt%, the geometric dilution method described by Banovic [20] was used to determine the nominal composition. Banovic [20] found that compositions of deposits measured by geometric dilution had good correlation (±2.4 wt%) to that measured by EPMA. Concentration measurements were made with the EPMA when a higher degree of precision was required. Quantitative image analysis was used to perform geometric dilution and area fraction measurements. Area fraction was assumed equivalent to volume fraction. Twenty fields of view were measured for each deposit to provide good statistical confidence in the area fraction measurements.

Results

Steel–Cu deposits ranging in composition from 3.5 wt% to 97.0 wt% Cu were produced. The cracking susceptibility results for the steel–Cu deposits are summarized in Fig. 1 with solid and dashed lines corresponding to crack free and cracked deposits, respectively. Deposits with Cu concentrations up to 4.7 wt% Cu and greater than 51 wt% Cu were crack free. Solidification cracking was observed in deposits with Cu concentrations between 5.4 and 43.3 wt% Cu. The cracking susceptibility of deposits with Cu concentrations between 43.3 and 51 wt% Cu is unknown because there were no samples fabricated within this composition range.

Figure 3 is a micrograph of a 3.5 wt% Cu deposit. This deposit was crack free and remnants of the cellular solidification microstructure are apparent with bainite or martensite forming by solid state

Table 1 Compositions of AISI 1013 bar and DEOX Cu wire

	C	Mn	Si	S	P	Cr	Ni	Mo	Cu	Fe	Al	Sn
Cu wire	–	0.18	0.23	–	0.01	–	–	–	98.78	–	–	0.8
SAE 1013 Bar	0.13	0.82	0.173	0.02	0.007	0.026	0.066	0.015	0.08	98.643	0.009	0.011

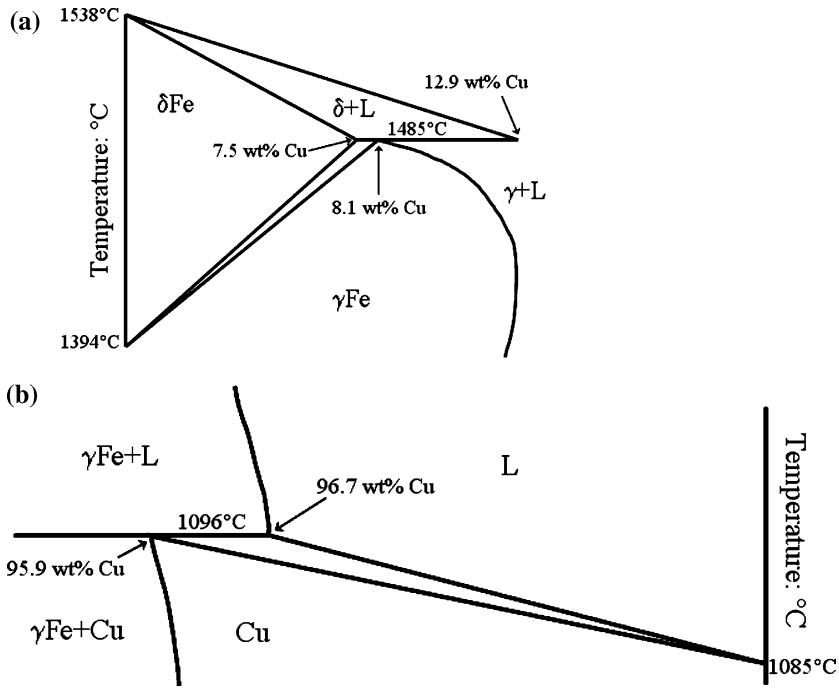

Fig. 2 Schematics of (**a**) Fe rich and (**b**) Cu rich peritectics adapted from Fe–Cu phase diagram [18]

transformation due to the rapid cooling rate. The equilibrium solidification sequence for this Cu concentration would be liquid to delta ferrite. No Cu rich terminal phase was observed in this deposit.

A 6.1 wt% Cu deposit is shown in Fig. 4. The deposit exhibited solidification cracking and a second phase with a spherical morphology was observed in the intercellular regions. Figure 5 displays EDS spectra obtained from the secondary phase and surrounding matrix, which confirms that the intercellular spheres observed in Fig. 4 are indeed Cu rich. The X-ray excitation volume with a 20 kV accelerating voltage is approximately 1.5 μm in diameter, which is slightly larger than the spherical secondary phase and is most likely the reason why an Fe peak is observed in the EDS spectrum of the intercellular secondary phase. Sn is also observed in the Cu spheres due to the presence of Sn in the Cu wire (0.8 wt% Sn), which appears to partition to the Cu rich phase. The expected equilibrium solidification sequence is the same as the steel–3.5 wt% deposit, and the presence of Cu is not expected under equilibrium solidification conditions. The intercellular Cu indicates that the solidification conditions deviate from equilibrium, which will be discussed in more detail in the subsequent section.

As the copper concentration in the deposit increases, the microstructure changes from cellular to columnar dendritic. Figure 6 is a micrograph of a 17.0 wt% Cu deposit. Cracking is observed along Cu rich regions of the deposit. Another change in microstructure is observed as the Cu concentration is increased to 35 wt% Cu, as seen in Fig. 7. The microstructure formed is the result of liquid phase separation that precedes solidification, resulting in a spinodal microstructure [22–24]. Like the 17 wt% Cu deposit (Fig. 6), cracking is observed along the Cu rich regions of the deposit.

As the Cu concentration is increased, the spinodal microstructure becomes a fully interpenetrating network of Fe rich and Cu rich phases as seen in Fig. 8 for 51.6 wt% Cu. This deposit and subsequent deposits with higher Cu concentrations were crack-free.

Figure 9 is a micrograph for 61.1 wt% Cu deposit that displays a combination of dendrites and liquid phase spinodal spheres in a Cu rich matrix. There is a change in the spinodal microstructure from interpenetrating networks to spheres that exhibit a secondary phase separation similar to that reported by Elder [23].

Discussion

Solidification behavior

Solidification conditions and the nominal composition control the solidification temperature range and amount of terminal liquid. Solidification cracking susceptibility is a function of the two latter quantities. Therefore, to understand cracking susceptibility it is necessary to determine the solidification behavior. Solidification behavior is bounded by equilibrium

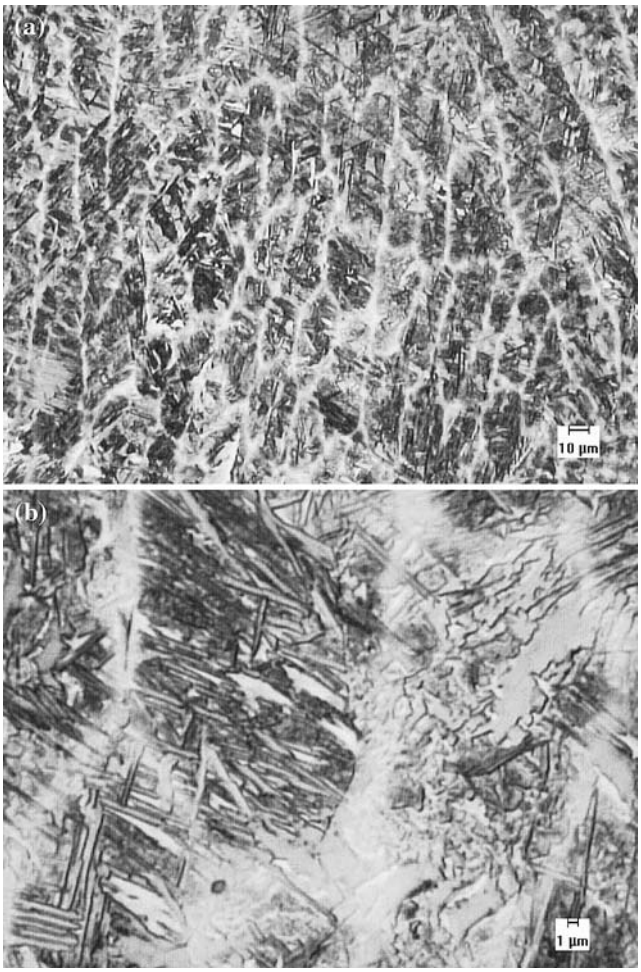

Fig. 3 (**a, b**) LOM photomicrographs of steel–3.5 wt% Cu deposit

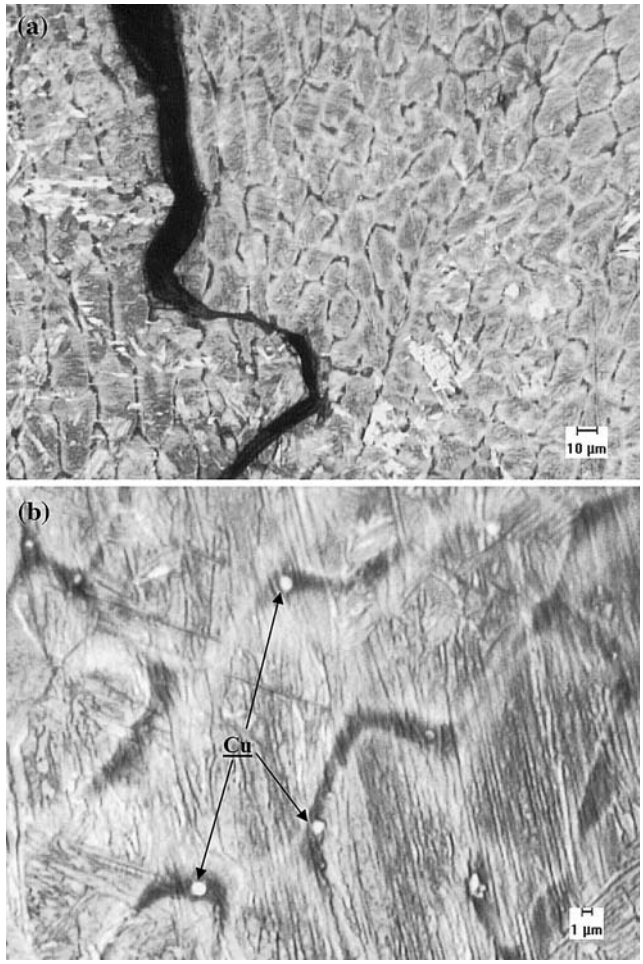

Fig. 4 (**a**, **b**) LOM photomicrographs of steel–6.1 wt% Cu deposit

and non-equilibrium (Scheil) conditions. These two solidification conditions can be used to determine the upper and lower bounds for the amount of terminal liquid and the solidification temperature range.

To determine the solidification behavior of Fe–Cu alloys, and determine the amount of terminal Cu rich liquid that would form during solidification, the dimensionless back diffusion coefficient α must be calculated. Once the solidification behavior is known, the solidification temperature range and amount of terminal liquid can be determined.

It has been shown that microsegregation in welds is a function of the back diffusion potential of solute elements in the solidifying solid as the weld freezes [17, 22–25]. Alloy systems with a small back diffusion potential will experience greater levels of microsegregation during solidification. The greater microsegregation will produce a larger amount of terminal solute rich liquid, which will impact the solidification cracking susceptibility of the alloy system.

In order to determine the solidification condition, the dimensionless back diffusion parameter (α) was calculated for the Fe–Cu system using the 6.1 wt% deposit. This sample will provide an upper bound estimate because the primary solidification phase is δFe, as it has a greater diffusivity of Cu than γFe [26]. Following the Brody and Fleming [25] solidification model, α is given by

$$\alpha = \frac{D_s t_f}{L^2} \tag{1}$$

where D_s is the diffusivity of the solute (Cu) in the solid (δ or γ Fe), t_f is the solidification time and L is the distance the solute must travel to eliminate any compositional gradient.

Because diffusivity is dependant on temperature and crystal structure of the solvent phase, the value of the back diffusion potential will change as the deposit cools. Therefore, an upper bound estimation is made

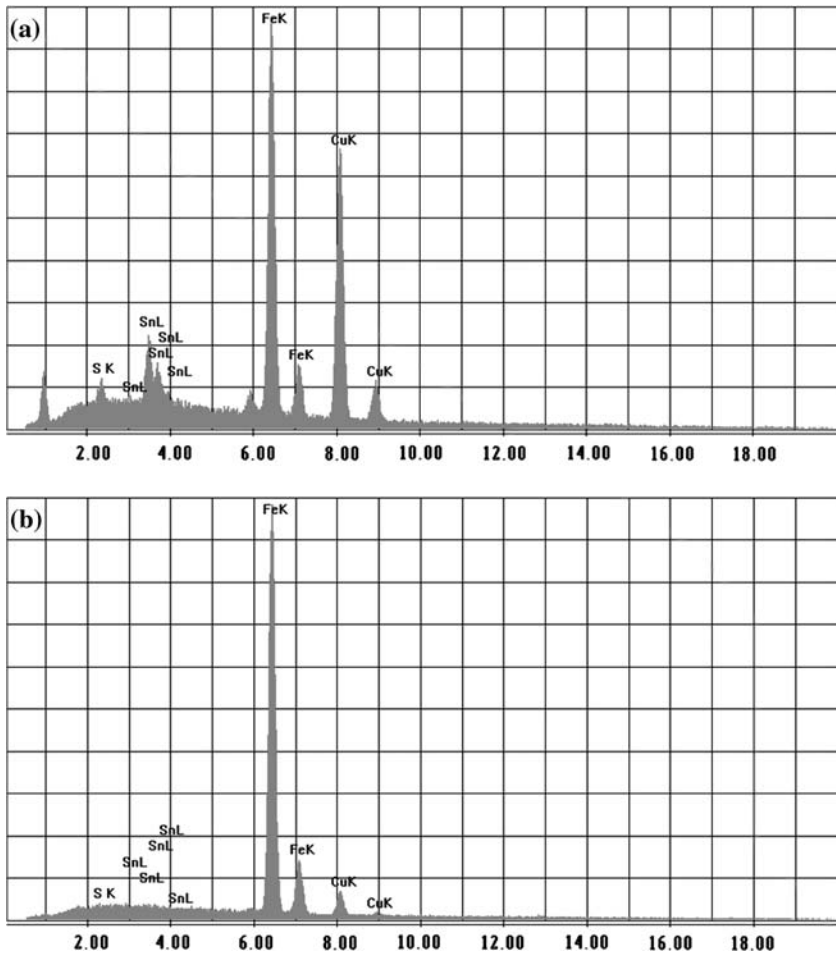

Fig. 5 EDS spectra of (**a**) intercellular sphere, (**b**) surrounding matrix, from steel– 6.1 wt% Cu deposit

for the back diffusion potential (α_{max}) of the 6.1 wt% Cu sample. If α_{max} is found to be $\ll 1$, then the Fe–Cu alloys are expected to solidify under non-equilibrium conditions.

Diffusivity of Cu in δFe was found to be 7.9×10^{-12} (m^2/s) at 1500 °C [26]. This data provides an upper bound value for the diffusivity of Cu in δ Fe over the relatively narrow temperature range for δ Fe (1515–1485 °C). As the 6.1 wt% alloy continues to cool, the γ Fe begins forming from the liquid at 1485 °C. To provide the highest possible back diffusion potential in γFe, the diffusivity was calculated at the peritectic temperature, 1485 °C, to be 7.6×10^{-14} (m^2/s) using the diffusion data provided by Arita [26].

L is equivalent to half the dendrite arm spacing since this represents the distance the solute atoms must travel to eliminate any concentration gradients in the forming solid. The average dendrite arm spacing was found to be 9.5 μm for the 6.1 wt% Cu sample.

Assuming a linear cooling rate during solidification, the solidification time, t_f, can be determined with the following equation:

$$t_f = \frac{\Delta T}{\varepsilon} \tag{2}$$

where t_f is the solidification time, ΔT is the solidification temperature range and ε is the cooling rate.

To provide an upper bound estimate of the back diffusion potential in δFe, the temperature range (ΔT) between the liquidus and the Fe rich peritectic in the 6.1 wt% Cu alloy (1515 and 1485 °C) was used. Assuming the 6.1 wt% Cu alloy solidified under non-equilibrium conditions, back diffusion of Cu solute atoms would occur in γ Fe at temperatures below the Fe rich peritectic (1485 °C). The largest ΔT for γ Fe, which will result in the greatest amount of time for back diffusion, is the peritectic temperature (1485 °C) minus the Cu rich peritectic isotherm (1096 °C).

To estimate the cooling rate the Rosenthal equation for three dimensional heat flow from a point heat source was utilized [27]. This is reasonable because transverse metallographic cross-sections of the weldments revealed a semi-circular weld pool shape, which is indicative of 3-D heat flow. This was expected

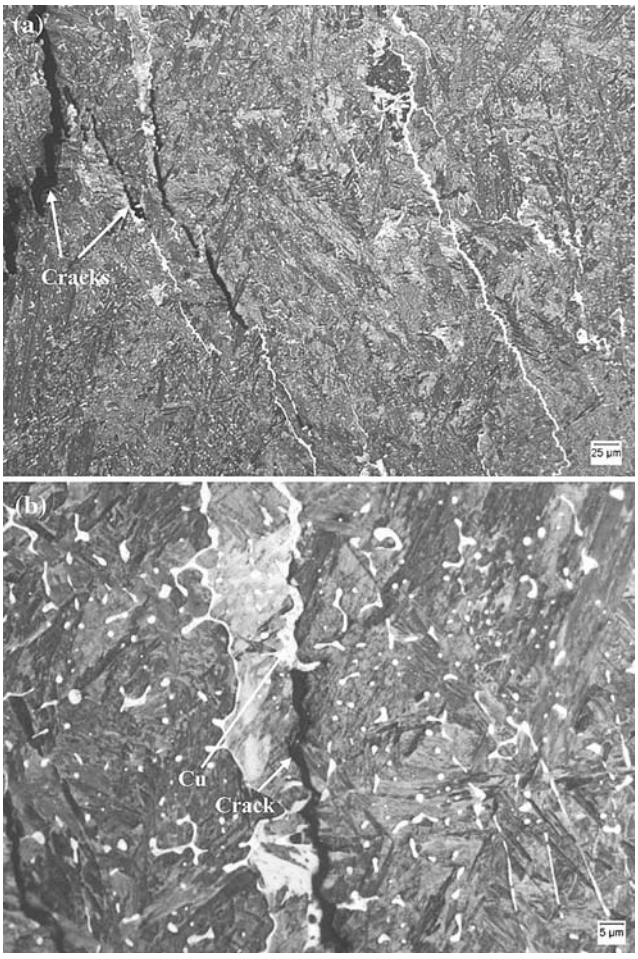

Fig. 6 (**a**, **b**) LOM photomicrographs of steel–17 wt% Cu deposit

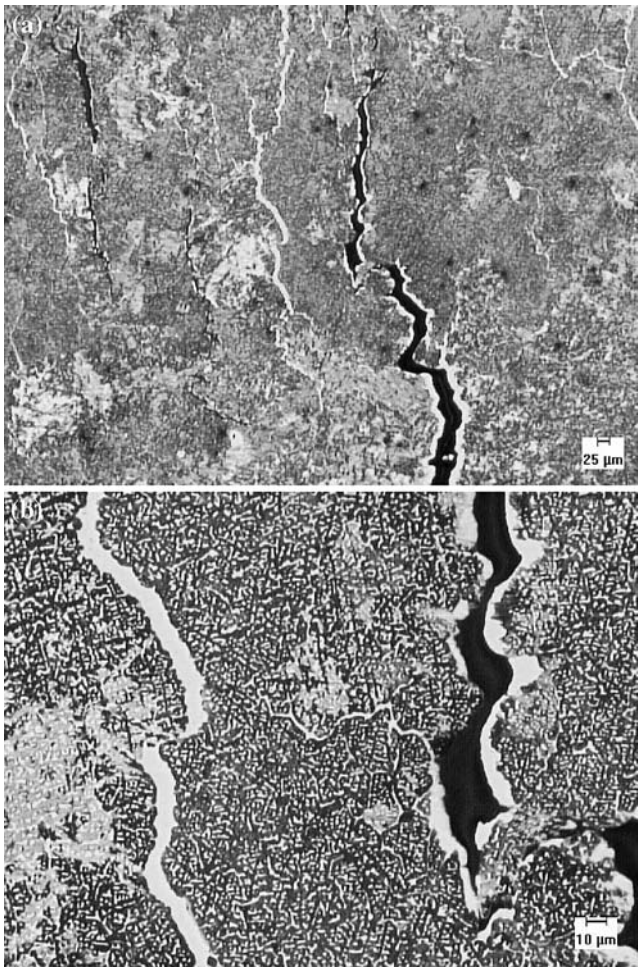

Fig. 7 (**a**, **b**) LOM photomicrographs of steel–35 wt% Cu deposit

because the rolled steel bars were secured along three sides in a large jig for welding. Along the weld center line, the Rosenthal equation simplifies to:

$$\frac{\partial T}{\partial t} = \frac{2\pi\lambda S(T - T_0)^2}{\eta_a VI} \tag{3}$$

where λ is the thermal conductivity, S is the travel speed, T is the temperature at which the cooling rate is estimated, T_0 is the pre heat temperature, η_a is the arc transfer efficiency and VI is the arc power. The thermal conductivity for Fe at 727 °C is 0.326 W/(cm °C), which was used as the effective thermal conductivity. For the conditions used to make the deposits, VI = 2500 W, S = 0.2 cm/s, T_0 = 25 °C, T = 1515 °C (the liquidus temperature for the 6.1 wt% Cu alloy) and η_a = 0.75 for the GTAW process [28]. Given the above conditions, the approximated cooling rate was found to be 485 °C/s. For solidification as primary δFe, the solidification temperature range is 45 °C, resulting in a solidification time of 0.09 s. Given the dendrite arm spacing of 9.5 μm, the resultant α = 0.0054, which is $\ll 1$, therefore back diffusion is negligible. If the primary solid was γFe, the maximum solidification temperature range would be 389 °C, which is the Fe rich peritectic temperature (1485 °C) minus the lower Cu rich peritectic temperature (1096 °C). The estimated cooling rate would be 466 °C/s, and the solidification time would be 0.83 s. Then α = 0.0007, which is also $\ll 1$ and even smaller than the back diffusion coefficient for solidification as primary δFe. Even though the solidification time is greater for γFe, the diffusivity is nearly two orders of magnitude less than that for δFe. Therefore, negligible back diffusion will occur during solidification, indicating that the solidification conditions are expected to be close to non-equilibrium ''Scheil'' conditions.

It should be noted that the cooling rate is an estimate for two reasons. First, the Rosenthal solution is based on the assumption of a point heat source. In

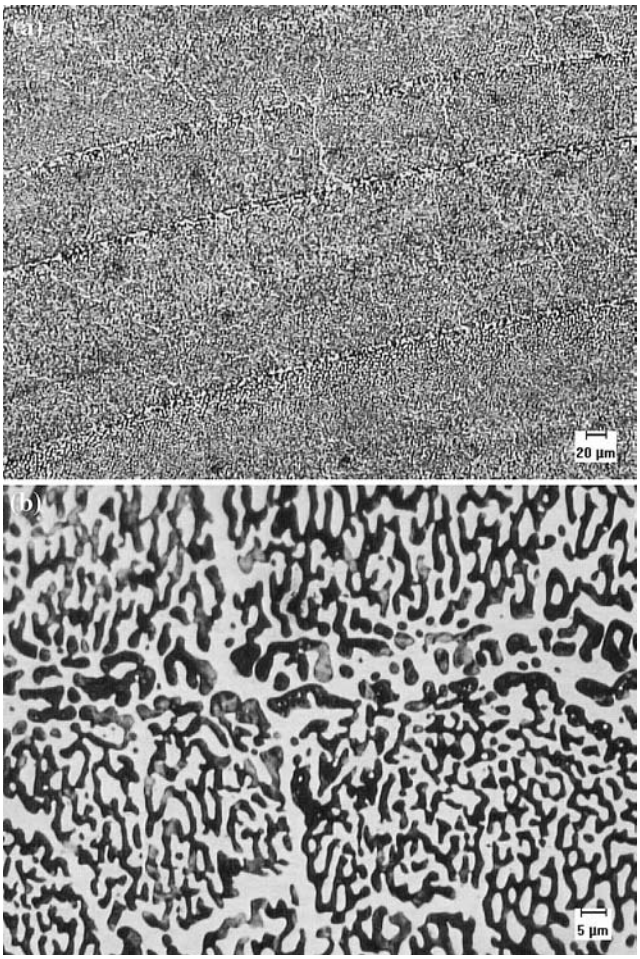

Fig. 8 (**a, b**) LOM photomicrographs of steel–52 wt% Cu deposit

practice, the GTAW heat source is not a point heat source but rather, more diffuse, which will result in lower cooling rates. Secondly, cooling rate is a function of temperature. The cooling rate decreases with decreasing temperature. Assuming the actual cooling rate is only half that predicted by the Rosenthal equation, α_{max} for δ and γ Fe are 0.011 and 0.0014 respectively. Non-equilibrium conditions persist even if cooling rate is decreased by half.

As such, it can be concluded that the presence of the copper spheres in the 6.1 wt% sample (Fig. 4) is a result of non-equilibrium solidification conditions. However, the absence of terminal Cu in the steel–3.4 wt% Cu sample (Fig. 3) is evidence that some back diffusion of Cu did occur to prevent the formation of terminal Cu at this nominal composition. Based on these two microstructures, and the back diffusion calculations, the solidification conditions are close to non-equilibrium, but some limited diffusion does exist.

The solidification behavior of the 6.1 wt% Cu alloy is representative of the solidification behavior for the entire Fe–Cu system. This can be seen by considering how the parameters that effect α vary with Cu concentration. If Cu concentration is increased slightly beyond 6.1 wt%, the solidification temperature range in δFe decreases. This will decrease α for concentrations up to 8.1 wt% Cu, which is the maximum concentration at which the primary solid phase is δFe. For Cu concentrations greater than 8.1 wt%, the primary solidification phase changes from δ to γFe and resultant diffusivity decreases by nearly two orders of magnitude, thereby significantly reducing α. This is true even though the solidification temperature range, which effects solidification time, is greater in γFe than it is in δFe. As Cu concentration is increased beyond 8.1 wt%, the solidification temperature range decreases, further reducing the back diffusion potential of Cu in Fe. Given the effects of increasing Cu concentration on t_f, and D_s, the entire Fe–Cu system is expected to exhibit near Scheil solidification conditions.

Assuming the solidification conditions are non-equilibrium for all steel–Cu alloys, there will be an even greater range of nominal compositions with large solidification temperature ranges. The influence of Cu concentration and solidification conditions on solidification temperature range is shown in Fig. 10. Under equilibrium conditions the solidification temperature range is quite small up to the Fe rich peritectic (8.1 wt% Cu). As the nominal composition of Cu increases beyond 8.1 wt% the equilibrium solidification temperature range is less straightforward due to the shape of the γ solidus. Because the austenite solidus extends out to approximately 13 wt% Cu before bending back to 8.2 wt% Cu, the equilibrium solidification sequence will occur by initial solidification, followed by remelting, then resolidification at the Cu rich peritectic isotherm. This is the case for equilibrium solidification of alloys with nominal Cu concentrations ranging from approximately 8 wt% to 13 wt%. In Fig. 10, the line representing the equilibrium solidification temperature range ignores the initial solidification and remelting phenomenon, thereby displaying an upper bound range of compositions with a solidification temperature range on the order of hundreds of degrees C. The solidification temperature range for equilibrium and non-equilibrium solidification conditions will be approximately the same (within ~10 °C) when the nominal composition of the deposit is greater than approximately 13 wt% Cu. With Scheil solidification conditions, the range of nominal compositions with solidification temperature range on the order of several hundred degrees C is increased to even trace

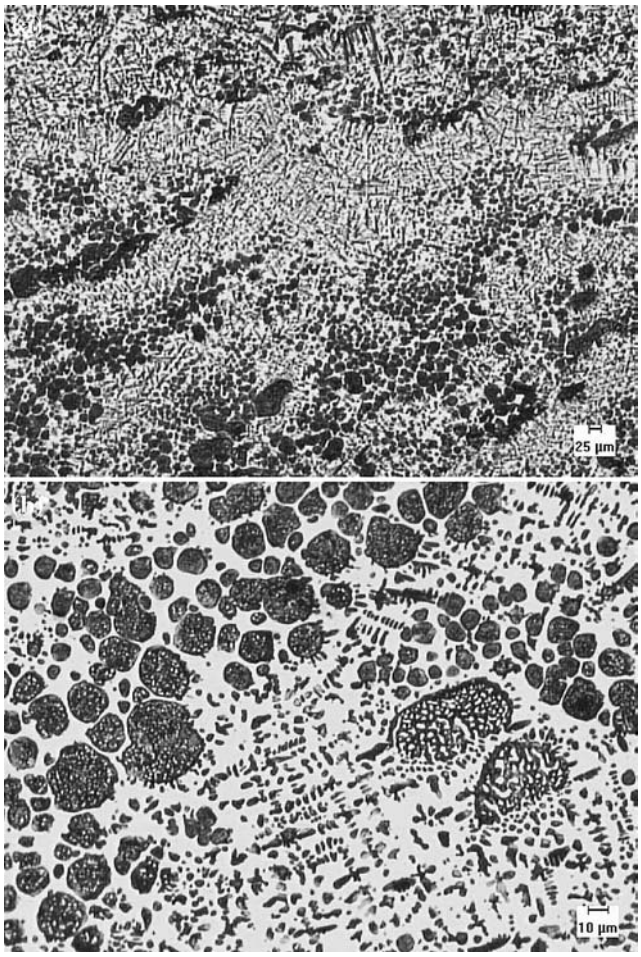

Fig. 9 (**a, b**) LOM photomicrographs of steel–61 wt% Cu deposit

amounts of Cu. This is because the terminal reaction during non-equilibrium solidification is pure Cu over the entire range of nominal compositions in the binary phase diagram.

Figure 10 also displays the range of nominal compositions that experienced solidification cracking, which correlates reasonably well with the range of compositions where the solidification temperature range is very large. At approximately 43 wt% Cu another factor comes into play, the amount of terminal liquid available for backfilling of cracks.

The amount of terminal liquid is the other key variable in solidification cracking susceptibility. The terminal liquid is defined as the volume of liquid present at the end of solidification. This terminal liquid transforms to the Cu rich phase at the end of solidification. The amount of terminal liquid can be determined by measuring the amount of Cu rich phase in the deposits. The volume fraction measurements for the deposits are presented in Fig. 11. The 95% confidence interval was used to calculate error bars for each point. Cracking was observed in deposits that contained between 0.1 and 27 vol.% terminal Cu.

Given that the deposits solidify under non-equilibrium Scheil conditions, the measured amount of terminal Cu can be compared to the predicted amount as calculated by the Scheil equation. To predict the amount of terminal Cu the differential form of the Scheil equation must be used because the equilibrium partitioning coefficient, k, is not constant in the Fe–Cu system. The differential Scheil equation is given by

$$\mathrm{d}f_S = \left(\frac{1 - f_S}{C_L - C_S^*}\right)\mathrm{d}C_L \tag{4}$$

where $\mathrm{d}f_S$ and $\mathrm{d}C_L$ are the infinitesinamal change in fraction solid and liquid composition respectively. C_L and C_S^* are the composition of the liquid and the solid, respectively, at the solid/liquid interface at any temperature given by the equilibrium liquidus and solidus lines from the Fe–Cu phase diagram. Equation 4 enables the fraction solid (and corresponding fraction liquid) to be calculated by use of a finite difference method for any given nominal composition.

When using the finite difference method, the starting conditions are: $f_S = 0$, $C_L = C_O$ at the liquidus temperature, and C_S^* is given by the solidus composition at the liquidus temperature. The value of $\mathrm{d}C_L$ was set to 1 wt% Cu. The values for C_L and C_S^* are read directly from the equilibrium phase diagram. The fraction solid formed at any temperature below the liquidus is found by repeatedly solving Eq. 4 for each $\mathrm{d}C_L$ and summing the resultant values of $\mathrm{d}f_S$ to provide fraction solid at any temperature. The finite difference technique provides the mass fraction of solid (f_S). The mass fraction liquid, f_L, is then given by $f_L = 1 - f_S$. For

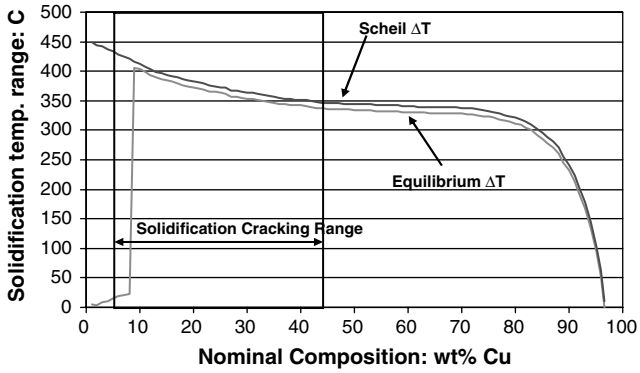

Fig. 10 Solidification temperature range for equilibrium and Scheil solidification conditions. Crack susceptible range of compositions indicated by arrow

the case of the Fe–Cu system, the differential Scheil calculation was carried out until the Cu rich peritectic isotherm was reached since all liquid that reaches the Cu rich peritectic (96.7 wt% Cu) will be transformed to the Cu rich phase (95.9 wt% Cu and greater). This can be seen in the Fe–Cu phase diagram in Fig. 1.

To determine the volume percent terminal Cu for Scheil solidification conditions, the f_L, which is in weight fraction, must be converted to volume percent by a modification of the lever rule:

$$V_{Cu} = \frac{(f_{L,Cu}/\rho_{Cu})}{(f_{L,Cu}/\rho_{Cu}) + (f_{S,Fe}/\rho_{Fe})} \times 100 \quad (5)$$

where $f_{L,Cu}$, $f_{S,Fe}$, ρ_{Cu} and ρ_{Fe} are the weight fraction and room temperature density of Cu and Fe respectively. Using Eq. 5, the resultant values for volume percent terminal Cu as predicted by the differential form of the Scheil equation are presented in Fig. 12 as the ''Scheil Solidification Model'' line. The volume fraction terminal liquid can be determined using the finite difference Scheil technique given the assumption that the equilibrium phase boundary lines are known and that the solidifying liquid follows these boundaries as it is cooled. This is expected to provide a good approximation for Cu concentration between 3.5 and 22.5 wt%. The presence of a liquid phase spinodal decomposition in deposits with Cu concentration 35 wt% and greater results in a change of phase boundary lines that does not allow the iterative Scheil technique to be used. The liquid phase spinodal decomposition will be discussed more in the next section. Also in Fig. 12 are the measured values of Cu rich phase from deposits with Cu concentration up to 22.5%, with error bars that represent the 95% confidence interval for both composition measurements with the EPMA and volume fraction measurements with QIA.

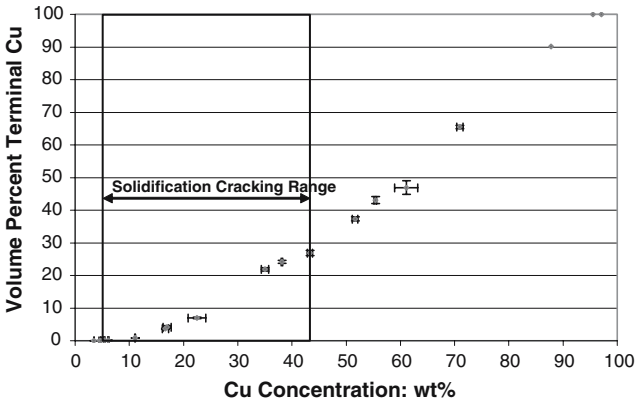

Fig. 11 QIA measured amounts of terminal Cu. Crack susceptible range of compositions indicated by arrow

Additionally, the expected amount of terminal Cu under equilibrium solidification conditions, assuming all subsequent diffusion ceased at the end of solidification, is presented as the ''Equilibrium Solidification'' line. These results are determined by the lever rule at the Cu rich peritectic isotherm temperature (1096 °C) to determine the fraction terminal Cu rich phase. In this calculation, the Fe rich solid phase was taken from the equilibrium phase diagram to be 8.2 wt% Cu and the Cu rich liquid phase was given by 96.7 wt% Cu. The liquidus composition at the Cu rich peritectic (96.7 wt%) was used to represent the amount of terminal Cu because all liquid that reaches the Cu rich peritectic isotherm will transform to the Cu rich solid phase. The weight fraction terminal rich Cu was then converted to volume percent using Eq. 5.

The second equilibrium line, ''Room Temp Equilibrium'', displays the room temperature volume percent of Cu as determined by the equilibrium binary Fe–Cu phase diagram at room temperature. These values were calculated with data from the Fe–Cu phase diagram at 600 °C, which shows negligible solid solubility of Fe and Cu in each other.

The unique shape of the Fe–Cu phase diagram produces an unexpected result in the solidification modeling as seen in Fig. 12. For any nominal composition greater than the Fe rich peritectic (8.1 wt% Cu) non-equilibrium solidification results in less terminal Cu rich liquid than for equilibrium solidification conditions. This is due to the shape of the γ solidus line. As an alloy cools below the Fe rich peritectic temperature, the solid solubility of Cu in austenite increases to approximately 14% at 1400 °C. However, below this temperature, during equilibrium solidification, the entire solid begins rejecting Cu solute into the liquid. In the Scheil condition, Cu solute is ''locked'' into the pre-existing solid due to the negligible diffusivity of Cu in austenite. The result is less Cu solute present to form terminal liquid in the Scheil condition.

In simple binary eutectic systems, the opposite effect occurs, with Scheil conditions acting as an upper bound for the amount of terminal liquid [17]. In a eutectic system, the solidus and liquidus slopes are of the same sign over the entire solidification temperature range and the composition of the solid continues to increase until the maximum solid solubility is reached at the eutectic isotherm. This results in the largest amount of solute being rejected into the liquid when solidification occurs under Scheil conditions. In the Fe–Cu system the solidus and liquidus slopes are no longer of the same sign over the entire solidification temperature

range. The solidus slope starts negative then becomes positive as temperature decreases while the liquidus slope remains negative. The result is a decreased amount of terminal Cu rich phase when solidifying with Scheil conditions.

The significance is that both the equilibrium and Scheil solidification calculations predict less solid Cu rich phase at room temperature than the equilibrium room temperature results. This is due to the assumption that there is no diffusion of Cu in Fe at the end of solidification, which was made in both the Scheil and Equilibrium solidification models.

Because the Fe–Cu system has a low back diffusion potential, it is expected that both the equilibrium room temperature and equilibrium solidification calculations would not accurately predict the amount of terminal second phase. This is supported in Fig. 12 since there is reasonably good agreement between the Scheil prediction and the experimental data. Yet there is a slight over prediction of the amount of terminal Cu using the Scheil calculation compared to the measured volume percent for any given nominal composition. There are two possible reasons for this. First, the deposits fabricated in this work contains elements other than Fe and Cu, therefore, the phase boundary lines for the steel–Cu deposits may be shifted as compared to the binary Fe–Cu system. Secondly, dendrite tip undercooling can enrich the composition of the first solid to form, resulting in less terminal solute rich liquid than predicted by the Scheil results [29]. To investigate this possibility, an EPMA line scan across the cellular structure in the steel–6.1 wt% alloy was acquired (Fig. 13). The line scan spans the cellular structure and intersects with a terminal Cu rich sphere. Because the size of the sphere is approximately the same size as the X-ray emission volume, it is not possible to quantitatively determine the composition of the interdendritic Cu rich phase with the EPMA technique, however, the composition profile across the cell can provide information on how the composition of the solid changed during solidification. The portion of the EPMA line scan in Fig. 13 representing the cell core to the intercellular region is shown in Fig. 14 and is plotted as a function of normalized distance from the cell core to the cell boundary. This experimental data is compared to the Scheil calculations where the cell core is taken as $f_S = 0$ and the interdendritic region, where the Cu concentration peaks, is taken as $f_S = 1$. Note that the experimental data has a higher Cu concentration than that predicted by the Scheil model for any amount of fraction solid (4.8 vs. 3.8 wt% Cu, respectively). This is most likely a result of dendrite tip undercooling, a shift in phase boundary lines, back diffusion, or a combination of the three.

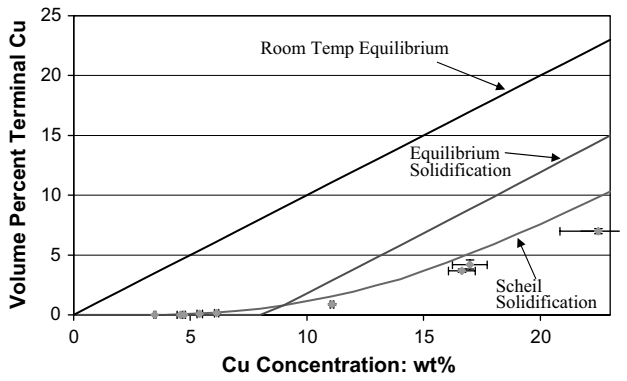

Fig. 12 Volume percent terminal Cu calculated under several different conditions compared to QIA measured amounts of terminal Cu

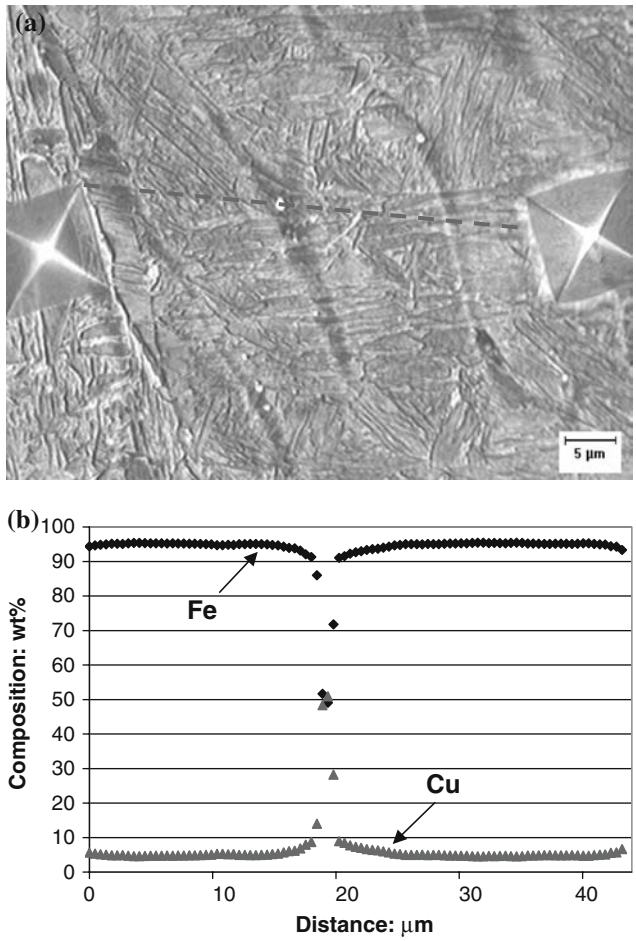

Fig. 13 (**a**) LOM photomicrograph of steel–6.1 wt% Cu deposit with (**b**) EPMA line scan across cells and Cu rich intercellular region

The amount of undercooling (ΔT) required to cause this increase in dendrite core concentration can be estimated using Fe–Cu phase diagram and the following relationship:

$$\Delta T = m_s \Delta C \tag{6}$$

where m_S is the slope of the δFe solidus (–6.54) and ΔC is the difference in Scheil predicted and EPMA measured dendrite core concentrations, which is ~1 wt% for the case of the 6.1 wt% Cu alloy. The undercooling necessary to cause the observed enrichment of Cu is ~6.5 °C. This may be the result of tip undercooling, which can be estimated using the following expression derived by Burden and Hunt [30], which assumes that the growth occurs at the minimum undercooling:

$$\Delta T = \frac{G_L D_L}{R} + 2^{3/2}\left[\frac{-\Gamma m_L R C_0 (1-k)}{D_L}\right]^{1/2} \tag{7}$$

Table 2 contains a description of the terms used in Eq. 7. Published values for Γ and D_L for δFe–Cu are unavailable, therefore published values for δFe–C were used [31]. The temperature gradient can be estimated directly from the Rosenthal solution via

$$G_L = \frac{\varepsilon}{S} \tag{8}$$

where ε is the cooling rate, estimated using Eq. 3 above to be 485 °C/s, and S is the heat source travel speed (2 mm/s). The amount of undercooling is a function of growth rate, which varies in the weld pool from zero at the fusion line-base metal interface to approximately the travel speed at the weld centerline (ignoring crystallographic growth effects). Use of Eq. 7 with a calculated temperature gradient of 243 °C/mm indicates that a growth rate of 1.3 mm/s will result in a ΔT of ~ 6.5 wt% Cu. This required growth rate is very similar to the heat source travel speed used to prepare the deposits and indicates that the difference in EPMA measured and Scheil calculated dendrite core concentrations can generally be attributed to dendrite tip undercooling.

Table 2 Terms used in calculation of undercooling

Term	Definition	Value
R	Growth rate	Varies from 0 to ~ travel speed (mm/s)
G_L	Temperature gradient in the liquid = ε/R	Varies with R (°C/mm)
D_L	Diffusivity of solute in the liquid	2×10^{-8} m^2/s for δFe–C [31]
Γ	Gibbs–Thomson parameter	1.9×10^{-7} mK for δFe–C [31]
m_L	Liquidus slope	–4.11
C_o	Nominal composition	Fe–6.1 wt% Cu
K	Equilibrium distribution coefficient	0.63

Liquid phase separation

Another potential indicator of undercooling is the presence of liquid phase spinodal. According to the Fe–Cu binary phase diagram with metastable miscibility lines [32] (Fig. 15), a certain amount of undercooling is required for the liquid phase separation to occur. The amount of undercooling is dependent upon nominal composition. Liquid phase spinodal structures were seen for alloys ranging from 35 to 71 wt% Cu, which corresponds to a minimum undercooling ranging from 54 °C to 32 °C respectively. The amount of undercooling not only effects the composition of the first solid to form and whether the liquid phase separation occurs, it also decreases the solidification temperature range and solidification cracking susceptibility concomitantly.

As discussed in the Results section, there is a significant change in microstructure between the 17 and 35 wt% Cu deposits (Figs. 6 and 7 respectively). This provides one indicator of a liquid phase separation and subsequent spinodal decomposition in the Fe–Cu system, which has been reported by several researchers [33–35]. Another evidence is the composition of the Fe rich and Cu rich phases of the spinodal. EPMA measurements were made of the Fe and Cu rich phases of the spinodal microstructure and are given in Table 3. These results are in good agreement

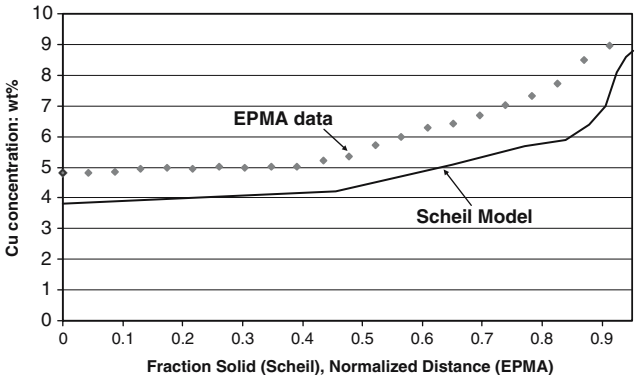

Fig. 14 Composition of Cu from the cell core to intercellular region in 6.1 wt% Cu sample compared to Scheil predicted composition

Table 3 Phase Compositions of spinodal structures

Nominal Composition	Phase	
	Fe rich wt% Cu	Cu rich wt% Cu
Steel–16.7 wt% Cu	11.3	92.5
Steel–35.0 wt% Cu	13.6	93.2
Steel–37.9 wt% Cu	12.7	90.8
Steel–50.5 wt% Cu	16.6	88.4
Steel–55.3 wt% Cu	15.5	94.8
Steel–69.5 wt% Cu	17.7	92.1

with the experimental results of Nakagawa [33] and Elder et al. [34] as compiled by Chen and Zin [36].

There are two distinct types of liquid phase spinodal structures observed. The first type consists of an interpenetrating Fe rich and Cu rich networks that are continuous throughout the fusion zone. Fig. 8 is an example of this morphology, which is very similar to that observed by Zeng et al. [35], but with a larger wavelength due to the lower cooling rates in GTAW deposition as compared to laser surface alloying used by Zeng. This first structure was observed in deposits with nominal compositions ranging from 35.0 to 55.3 wt% Cu.

A second type of spinodal structure is seen as the nominal composition of Cu increases (Fig. 9), which correspond to spinodal structures observed by Elder [34]. Figure 16 is an SEM micrograph of a liquid phase spinodal sphere observed in the 61.1 wt% Cu deposit. EDS was used to determine that the matrix is Cu rich and the spheroid with perturbations is Fe rich with Cu rich spheres within the Fe rich outer ring (Fig. 17). All

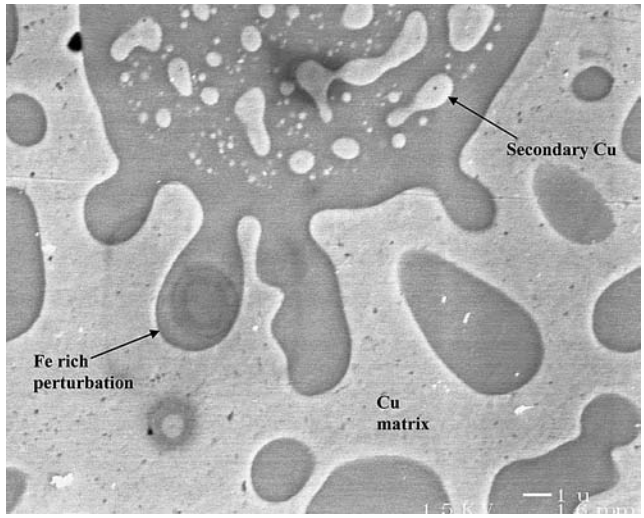

Fig. 16 SEM image using predominantly secondary electrons of a spinodal sphere in 61.1 wt% Cu deposit

three EDS spectra were taken under the same conditions for the same count time and are plotted on the same scale, allowing for qualitative comparisons to be made. The EDS spectra of the secondary sphere is nearly identical to that of the matrix, with only slightly more Fe and Mn, most likely due to the excitation of the surrounding Fe rich sphere. The morphology of this second type of spinodal structure providence some evidence on how the Fe–Cu liquid phase spinodal solidifies.

It has been suggested [34] that the solidification sequence would begin with the Fe rich liquid phase due to the greater undercooling this phase would experi-

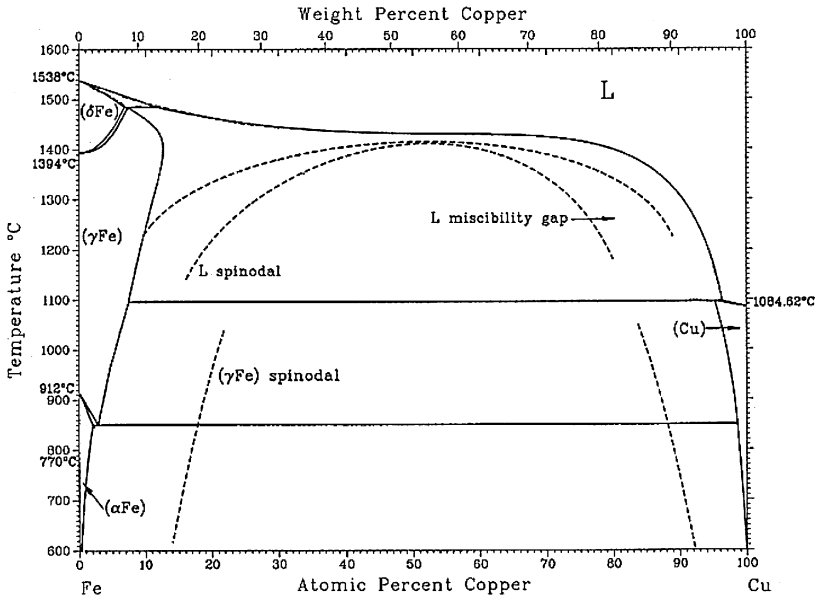

Fig. 15 Fe–Cu phase diagram with metastable miscibility lines [32]. Liquid phase separation will occur with undercooling over a large range of Cu concentration

ence at any given undercooling at the nominal composition. The solidification of the Cu rich phase would then follow. This hypothesis is supported by the spherical spinodal microstructures seen in Figs. 9 and 16. Fe rich perturbations are seen extending from the spheroid that has undergone secondary phase separation [34], where Cu rich spheres are seen within an Fe rich sphere surrounded by a Cu rich matrix. The presence of the Fe rich perturbations suggests that the Fe rich phase does indeed solidify first, with post liquid phase separation growth of the Fe rich phase into the Cu rich liquid phase.

Cracking susceptibility

The solidification cracking susceptibility of steel–Cu deposits can be understood by combining the solidification temperature range estimates (Fig. 10) and the volume percent terminal Cu data (Fig. 11). At Cu concentrations below approximately 5 wt% the estimated Scheil solidification temperature range is greater than 400 °C but no terminal Cu is observed. The absence of terminal Cu indicates that the deposit did not solidify completely under Scheil conditions and that there was some finite amount of back diffusion. The absence of terminal Cu also indicates that the solidification temperature range for deposits with less than 5 wt% Cu is less than that predicted using the Scheil solidification conditions. The deposit is crack free due to the lack of terminal Cu and most likely a reduced solidification temperature range.

The estimated solidification temperature range, under Scheil solidification conditions, for deposits with nominal Cu concentrations between approximately 5 and 43 wt% remains greater than 350 °C, and terminal Cu is present. The large solidification temperature range and intermediate amounts of terminal Cu produces solidification cracking. As the Cu concentration continues to increase beyond 43 wt%, the solidification temperature range continues to decrease and the amount of terminal Cu continues to increase. The increased terminal Cu is sufficient to backfill any cracks that may form during solidification [17].

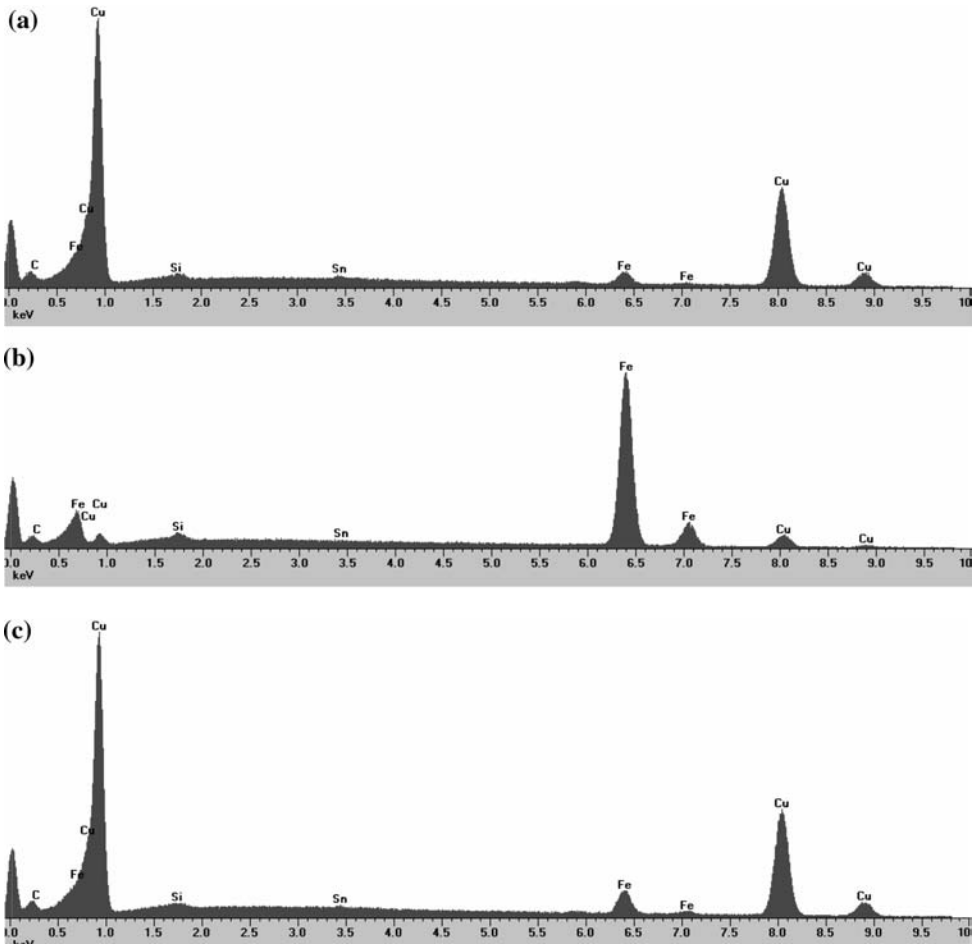

Fig. 17 EDS spectra of spherical spinodal structure: (**a**) matrix surrounding structure (**b**) Fe rich portion and (**c**) Cu rich portion of structure. All three spectra displayed with the same intensity scale

GTAW deposits may present a worst case cracking susceptibility scenario when compared to laser deposition. In work performed by Zeng, Cu was laser surface alloyed onto SAE 1045 steel producing a melt zone with nominal composition of 33 wt% Cu [35], in which no cracking was observed (D.W. Zeng, Pers. commun.). The same composition deposit fabricated using GTAW resulted in cracking, with the nominal composition lying well within the high crack susceptibility region. The microstructures observed in the current work are analogous to Zeng's but of a much coarser scale as would be expected due to slower relative cooling rate in GTAW processes as compared to laser surface alloyed composites.

In general, if Cu is to be deposited onto steel using arc welding processes, the first layer must contain at least 50 wt% Cu to avoid solidification cracking. A second potential solution is to use an interlayer material that exhibits good solid solubility and a small solidification temperature range when alloyed with Cu or Fe. The potential of using Ni as such an interlayer is explored in a future publication.

Conclusion

To determine the compositional cracking range of Cu in Steel, a wide range of steel–Cu deposits were fabricated by GTAW with a cold wire feed. EPMA measurements were carried out to determine the composition of the steel–Cu deposits. Deposits with compositions ranging from 5.4 to 43.3 wt% Cu were found to be crack susceptible, while compositions above 51.5 and below 4.7 wt% Cu were found to be crack free.

Solidification cracking was found to be a function of both the solidification temperature range and the amount of terminal Cu rich liquid. Cracking occurred when the calculated solidification temperature range for the Fe–Cu system was between approximately 350 °C and 435 °C and the measured amount of terminal Cu rich phase was between approximately 0.1 and 27 vol%. Solidification calculations utilizing a finite difference Scheil technique and the binary equilibrium Fe–Cu phase diagram provided reasonable estimates of the amount of terminal Cu during solidification. The current work may provide a more conservative estimate of solidification cracking susceptibility as compared to laser deposition.

Acknowledgments The authors gratefully acknowledge support of this work by the National Science Foundation through a PECASE Award, grant no. DMI 9983968, made through the Division of Manufacturing and Industrial Innovation of NSF.

References

1. *Thermal conductivity: metallic elements and alloys*, Touloukian YS (ed) Vol 1. IFI/Plenum, New York, Washington (1970)
2. Carpenter technology alloy Data: No. 883 (AISI H-13) tool steel
3. Engelmann P et al (1997) J Inject Mold Technol 1(1):18
4. Mazumder J. et al (1997) JOM 49(5):55
5. Knights M (2001) Plastics Technol 47(1):46, 49
6. Liu W, DuPont JN (2003) Scripta Mater 48(9):1337
7. Li XC, Stampfl J, Prinz FB (2000) Mater Sci Eng A: Struct Mater: Properties, Microst Process A282(1–2):86
8. Brice CA et al (2000) Mater Res Soc Symp Proc 625(Solid Freeform and Additive Fabrication):31
9. Noecker II FF, DuPont JN (2002) In: Solid Freeform Fabric Symp Proc pp 231–238
10. Asnis EA, Prokhorenko VM, Shvindlerman LS (1965) Welding Product 12(11):15
11. Vainerman AE, Osetnik AA (1968) Automated Welding 21(6):22
12. Cooper RB, Burns TH (1974) Metals Eng Quart 14(3):41
13. Dixon B (1981) Austr Welding J 26(4):23
14. Borland JC (1979) Welding Metal Fabric 47(1):19, 23, 28
15. Borland JC (1979) Welding Metal Fabric 47(2):99
16. Arata Y, Matsuda F, Katayama S (1977) Transa JWRI 6(1):105
17. Brooks JA (1990) In: Proc Mater Weldability Symp pp 41–47
18. Swartzendruber LJ (1990) In: Thaddeus HO, Massalski B, Subramanian PR, Kacprzak Linda (eds) Binary alloy phase diagrams. ASM International, Materials Park, Ohio, pp 1408–1410
19. Scheil E (1942) Zeitschrift fur Metallkunde 34/35:70
20. Banovic SW, DuPont JN, Marder AR (2001) Metall Mater Trans B: Process Metall Mater Proces Sci 32B(6):1171
21. Goldstein JI et al (1992) Quantitative X-ray analysis: theory and practice, in scanning electron microscopy and X-ray microanalysis. Plenum, New York and London, pp 417–523
22. DuPont JN (1999). Welding Res, Miami 78(7):253S
23. DuPont JN (1996) Metall Mater Trans A: Phys Metall Mater Sci 27A(11):3612
24. Clyne TW, Wolf M, Kurz W (1982) Metall Trans B: Process Metall 13B(2):259
25. Brody HD, Flemings MC (1966) Trans Metall Soc AIME 236(5):615
26. Arita M et al (1981) Metall Trans A: Phys Metall Mater Sci 12(3):497
27. Rosenthal D (1946) Trans ASME 68:849
28. DuPont JN, Marder AR (1996) In: Trends in Welding Research, proceedings of the international conference, 4th, Gatlinburg, Tenn., June 5–8, 1995, pp 449–454
29. Brooks JA, Baskes MI (1986) Adv Weld Sci Technol, Proc Int Conf Trends Weld Res, pp 93–99
30. Burden MH, Hunt JD (1974) J Crystal Growth 22(2):109
31. Kurz W, Fisher DJ (1989) Appendix 14, in Fundamentals of solidification. Switzerland, Germany, UK, USA, pp 293–294
32. Swartzendruber LJ (1994) In: Subramanian DJCPR, Laughlin DE (eds) Phase diagrams of binary copper alloys. ASM International, Materials Park, OH, pp 167–172
33. Nakagawa Y (1958) Acta Met 6:704
34. Elder SP, Munitz A, Abbaschian GJ (1989) Mater Sci Forum 50(Mater. Process. Space):137
35. Zeng DW, Xie CS, Yung KC (2002) Mater Lett 56(5):680
36. Chen Q, Jin Z (1995) Metall Mater Trans A: Phys Metall Mater Sci 26A(2):417